Finite volume method for three-dimensional transonic potential flow through turbomachinery blade rows

J. V. Soulis*

A finite-volume method has been developed for the calculation of transonic, potential flows through 3-D turbomachinery blades with complex geometries. The exact transonic potential flow equation is solved on a mesh constructed from small volume elements. A transformation is introduced through which cuboids of the physical plane are mapped into computational cubes. Two sets of overlapping volumes are used. While the thermodynamic properties are calculated at the primary volume centres, the flux balance is established on the secondary volumes. For transonic flows an artificial compressibility term (upwind density gradient) is added to density to produce the necessary directional bias in the hyperbolic region. The successive point over-relaxation Gauss–Seidel method has been used to solve the non-linear partial differential equations. Comparisons with experiments and/or other numerical solutions for various turbomachinery configurations show that the 3-D finite-volume approach is a relatively accurate, reliable and fast method for inviscid, transonic flow predictions through turbomachinery blade rows

Key words: *turbines, compressible flow, finite volume methods*

As a result of the rapid progress in numerical methods and in computer hardware the importance of computational fluid dynamics in the design of turbomachinery components is steadily increasing. Successful computational algorithms have evolved to solve the transonic full potential equation for 3-D isolated aerofoil flowfields. Existing wing transonic flow analysis codes with surface-fitted grids utilise co-ordinate transformations, Jameson[1], Holst[2], either analytical or numerical to map the flow domain surrounding the 3-D configuration into multiple finite-volumes. This approach is effective for relatively simple geometries. For geometrically complex turbomachinery configurations, Fig 1, analytical mesh-generations are difficult to apply. Hence, a simple but effective, entirely numerical, mesh-generation scheme is needed.

The numerical scheme is constructed on the same principles as the 2-D computational analysis described previously[3], in which a finite-difference scheme was developed from a second-order finite-element shape function which had been applied to arbitrary turbomachinery geometries using a body fitted non-orthogonal local co-ordinate system. A mesh was constructed from small cells which were packed around the turbomachinery blades and covered the whole blade-to-blade area.

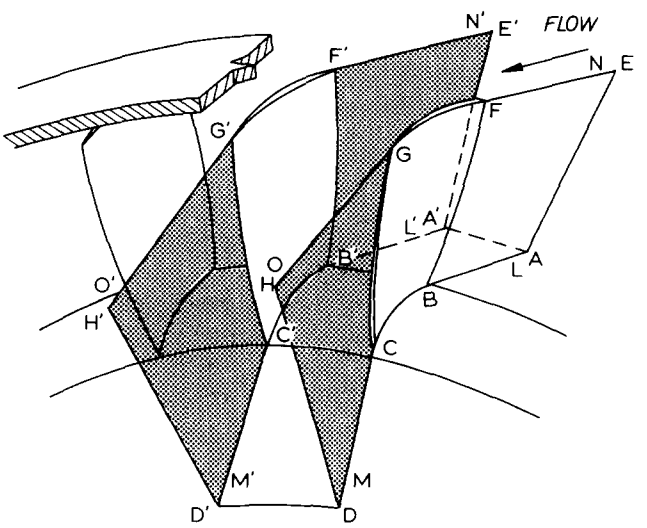

Fig 1 Schematic view of axial flow compressor blade row

To reduce the complexity of the numerical code in 3-D flow problems, a first-order finite-element is chosen so that the finite-difference scheme is relatively simple. The flow field is divided into cuboid blocks the structure of which are the same as the interior boundaries of the turbomachinery. A

* Whittle Laboratory, Department of Engineering, University of Cambridge, Cambridge, UK
Presently at Department of Civil Engineering, Demokrition University of Thrace, Komitini, Greece
Received 14 May 1982 and accepted for publication on 4 October 1982

 0142–727X/83/020085–12$03.00

local transformation is introduced through which the cuboids in the physical plane are mapped into computational cubes. The numerical scheme is constructed using two sets of overlapping cubes. All transformation matrices and coefficients as well as the flow quantities are defined at primary cube centres, while the potential is defined at primary cube vertices. The flux balance is then established on the secondary cubes. For locally supersonic zones, stability is achieved by the addition of an upwind artificial compressibility gradient ensuring a directional bias for any orientation of the velocity vector in the flow field. Converged solutions of the mixed-type non-linear equations are obtained using the Gauss–Seidel over-relaxation technique. A compromise is made between computer time and storage requirements.

The main features of the numerical scheme are that it preserves the practicability of the finite-element method of setting an irregular computational grid to fit a particular flowfield problem, and to modify it with ease if necessary, while it makes use of the simple mathematical analysis of finite-difference methods.

The 3-D algorithm was tested for several realistic turbomachinery problems comprising subsonic and transonic nozzle and cascade flows, and comparison is made with experiment and/or Denton's fully 3-D time-marching method[4].

Flow equations

The flow is assumed to be fully 3-D, inviscid, potential and steady but with no restriction to subsonic flow. Hence, the governing flow equations for the physical domain where the Cartesian co-ordinate system is introduced are:

$$\frac{\partial}{\partial x}(\rho u)+\frac{\partial}{\partial y}(\rho v)+\frac{\partial}{\partial z}(\rho w)=0,$$

$$u=\frac{\partial \phi}{\partial x}, \qquad v=\frac{\partial \phi}{\partial y}, \qquad w=\frac{\partial \phi}{\partial z}$$

$$q=(u^2+v^2+w^2)^{1/2}, \qquad T_{01}=\text{const.}, \qquad P_{01}=\text{const.} \tag{1}$$

$$\rho=\rho_{01}\left(1-\frac{q^2}{2C_pT_{01}}\right)^{1/\gamma-1}, \qquad p=p_{01}\left(\frac{\rho}{\rho_{01}}\right)^{\gamma}$$

$$\tilde{\rho}=\rho-\mu\rho_s\,\Delta s,\ \rho_s\,\Delta s=\frac{u}{q}\rho_x\,\Delta x+\frac{v}{q}\rho_y\,\Delta y+\frac{w}{q}\rho_z\,\Delta z$$

$$\mu=\max\left[0,\left(1-\frac{1}{M^2}\right)\mathrm{k}\right], \qquad \mathrm{k}=\text{const.},\ \text{typically of 1.6}$$

No assumption is made about the geometry of the blade row but the associated hub and casing surfaces are assumed to be surfaces of revolution.

The problem must be closed with a complete specification of the boundary conditions.

Upstream conditions

The stagnation pressure and temperature of the inlet flow are assumed to be constant throughout the flowfield; two inlet flow angles must be specified, one for the blade-to-blade and the other for the meridional plane. If instead of the inlet flow angles, the pitchwise velocity and spanwise angle are specified then blade rows with supersonic inlet flow can be calculated. An arbitrary value of the potential is also specified.

Notation

a	Local speed of sound, m/s
a_{ij}	Transformation weighting coefficients
C_p	Coefficient of specific heat at constant pressure, kJ kg^{-1} K^{-1}
G	Matrix of geometrical coefficients
g_{ij}	Elements of the G matrix
g^{ij}	Elements of the G^{-1} matrix
H	Transformation matrix from Cartesian to local ξ, η, ζ system
h	Determinant of the H matrix
i	Logical index of mesh variables along η direction $i=2$, IMP1
j	logical index of mesh variables along ξ direction $j=1$, JM
k	Logical index of mesh variables along ζ direction $k=2$, KMP1
k	Constant
M	Local Mach number
N	Number of blades
N_i	Shape functions $i=1, 2, 3, \ldots, 8$
P	Pressure, N/m^2
p	Pitch, m
Q	Total velocity in computational plane, m/s
q	Total velocity, m/s
R	Gas constant, kJ kg^{-1} K^{-1}
r	Radius, m
S	Entropy, kJ kg^{-1} K^{-1}
s	Co-ordinate along the stream direction, m
T	Temperature, K
U, V, W	Contravariant velocity components along the ξ, η, ζ directions, m/s
u, v, w	Cartesian velocity components along the x, y, z directions, m/s
x, y, z	Cartesian co-ordinates along the axial, pitchwise (swirl), spanwise (radial) directions, m
γ	Specific heat ratio
$\Delta\theta$	Angular distance between blades, rad
μ	Artificial compressibility
ξ, η, ζ	Transformed co-ordinate directions, m
ρ	Density, kg/m^3
ρhU, ρhV, ρhW	Mass fluxes along the ξ, η, ζ directions kg/s
ϕ	Velocity potential m^2/s

Subscripts

0	Stagnation value
1, 2	Upstream and downstream respectively

Downstream conditions

A value for the potential of one point on the downstream fluid boundary is estimated and this remains fixed throughout the iterations. Thus, the potential difference between the inlet and outlet flow boundaries determines a flowrate through the cascade, allowing the back pressure ratio to be specified independently regardless of whether the flow is choked.

Body surface conditions

In inviscid flow conditions the flow is tangent to a wall surface, thus the flow normal to the blade suction or pressure and/or to the endwall surfaces is zero:

$$q_n = \phi_n = 0 \tag{2}$$

In internal flow configuration problems, the inherent corner formation between hub or casing and suction or pressure surfaces requires special treatment. A major difficulty in solving the exact potential 3-D flow equation is the construction of sufficiently accurate discrete approximations to satisfy the various geometrical configurations at the solid boundaries. In turbomachinery where highly loaded blades and curved hub or casing surfaces are frequently encountered the accurate description of the solid boundary conditions is paramount to obtain satisfactory results.

Kutta-condition

For situations involving lifting the Kutta condition must be imposed at the trailing edges of the blades. Here, a vortex sheet potential jump, variable across the blade span, is calculated which will produce equal pressures on the suction and pressure blade surfaces in the vicinity of the trailing edge.

Periodical boundaries

Periodicity conditions are applied to the extensions from the blade surfaces, requiring the velocities to be identical at corresponding points of the two successive periodic planes. Upstream this is enforced by the requirement of a constant difference in potential; for a zero inlet tangential velocity this constant is also zero. Downstream from the trailing edges the potential differs by a quantity which is proportional to the circulation at that radius. On the same grid line this vortex sheet remains unchanged downstream from the trailing edges. Across the sheets, which are assumed to lie in the periodic blade extensions, the potential is discontinuous and the spanwise velocity is proportional to the gradient of the potential difference along the blade exit span.

For a Cartesian mesh the flow equations would require special finite-difference schemes near to the boundary, possibly resulting in interpolation schemes that can achieve only a low level of accuracy. The alternative approach of transforming the physical domain to a simple region is, in many cases, difficult especially for realistic bodies. Thus,

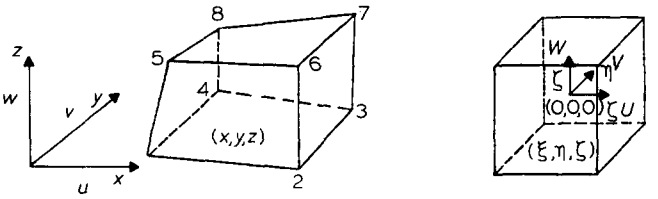

Fig 2 Distorted cubes are mapped into cubes

the flowfield must be divided into multiple blocks to accommodate all boundary surface discontinuities, slopes, and to provide good boundary fitting. This finite-element approach is very well adapted, therefore, to turbomachinery flows for the following reasons. A wide range of finite-elements is possible for adequate description of the surface boundaries of axial, mixed or radial flow machines. Minimal additional computational code logic is required for changing a particular element to a more sophisticated one. There is automatic treatment of the various forms of the applied boundary conditions. For an iterative approach these boundary conditions can be applied explicitly, i.e. from the previous iteration, and/or implicitly, i.e. initially established. Moreover, a single analysis can generate several finite-difference techniques which are dependent on the finite-element selection.

General transformation and numerical formulation

The discrete approximation to the governing flow equation has been developed by dividing the physical domain into cuboid cells which can be defined arbitrarily to produce surface-fitted grids the structure of which follows the turbomachinery internal configuration. Once this has been achieved a transformation is introduced through which cuboids of the physical domain are mapped into cubes of the computational domain. This transformation from global x, y, z Cartesian to local non-orthogonal ξ, η, ζ co-ordinates, shown in Fig 2, can be expressed as:

$$x = \sum_{i=1}^{8} N_i x_i \; y = \sum_{i=1}^{8} N_i y_i \; z = \sum_{i=1}^{8} N_i z_i \tag{3}$$

where N_i are the first-order, linear shape functions associated with the cuboid nodes. The use of the first-order shape functions has been determined by the necessity to restrict the complexity of the numerical code, which is inherent to almost all 3-D computational methods. The shape functions are defined in terms of the local non-orthogonal co-ordinate system as:

$$\begin{aligned}
N_1 &= 8(1/4-\xi/2)(1/4-\eta/2)(1/4-\zeta/2)\\
N_2 &= 8(1/4+\xi/2)(1/4-\eta/2)(1/4-\zeta/2)\\
N_3 &= 8(1/4+\xi/2)(1/4+\eta/2)(1/4-\zeta/2)\\
N_4 &= 8(1/4-\xi/2)(1/4+\eta/2)(1/4-\zeta/2)\\
N_5 &= 8(1/4-\xi/2)(1/4-\eta/2)(1/4+\zeta/2)\\
N_6 &= 8(1/4+\xi/2)(1/4-\eta/2)(1/4+\zeta/2)\\
N_7 &= 8(1/4+\xi/2)(1/4+\eta/2)(1/4+\zeta/2)\\
N_8 &= 8(1/4-\xi/2)(1/4+\eta/2)(1/4+\zeta/2)
\end{aligned} \tag{4}$$

Let $\boldsymbol{H}$ be the transformation matrix from the physical to the computational local co-ordinate system:

$$\boldsymbol{H} = \begin{vmatrix} x_\xi & x_\eta & x_\zeta \\ y_\xi & y_\eta & y_\zeta \\ z_\xi & z_\eta & z_\zeta \end{vmatrix} \tag{5}$$

Let $\boldsymbol{G}$ be the product $\boldsymbol{H}^T\boldsymbol{H}$ with elements g_{11}, g_{12}, g_{13}, g_{22}, g_{23}, g_{33} and also let $\boldsymbol{G}^{-1}$ be the inverse of matrix $\boldsymbol{G}$ with elements g^{11}, g^{12}, g^{13}, g^{22}, g^{23}, g^{33}. The contravariant velocity components U, V, W in the computational domain, which are parallel to ξ, η and ζ directions, respectively, are given as:

$$\begin{vmatrix} U \\ V \\ W \end{vmatrix} = \boldsymbol{G}^{-1} \begin{vmatrix} \phi_\xi \\ \phi_\eta \\ \phi_\zeta \end{vmatrix} \tag{6}$$

while the u, v, w velocity components in the physical domain are:

$$\begin{vmatrix} u \\ v \\ w \end{vmatrix} = \boldsymbol{H} \begin{vmatrix} U \\ V \\ W \end{vmatrix} \tag{7}$$

The continuity equation in the local non-orthogonal co-ordinate system[3] is:

$$\frac{\partial}{\partial\xi}(\rho hU) + \frac{\partial}{\partial\eta}(\rho hV) + \frac{\partial}{\partial\zeta}(\rho hW) = 0 \tag{8}$$

The physical interpretation of the quantities ρhU, ρhV and ρhW is that these are the mass fluxes across faces ξ = constant, η = constant and ζ = constant, respectively, of the finite volume, as shown in Fig 3. The computational mesh is generated so that blade and endwall boundaries coincide with faces of finite volumes adjacent to the boundary. Thus, the boundary conditions are $V = 0$ or $W = 0$, or a combination of these being zero on such a cell, hence greatly facilitating the treatment of solid boundaries.

A primary finite-volume or cell which is a cuboid in the physical plane or a cube in the computational plane is formed by eight nodes, as shown in Fig 2, while a secondary cell interlocks with eight primary cells, as shown in Fig 3. The centroid of the secondary cell, which is a grid itself, is assigned three indices i, j, k which change in the η, ξ, ζ directions, respectively. Shifts of plus or minus one of any of the indices yields the centroid of the next secondary cell while the local co-ordinates are in the range:

$$-\tfrac{1}{2} \leq \xi \leq \tfrac{1}{2}, \qquad -\tfrac{1}{2} \leq \eta \leq \tfrac{1}{2} \quad \text{and} \quad -\tfrac{1}{2} \leq \zeta \leq \tfrac{1}{2}$$

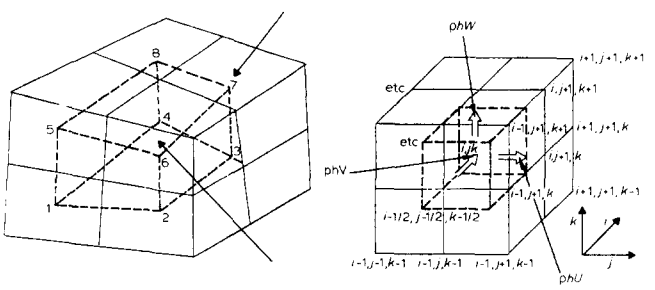

Fig 3 A secondary cell (cuboid) interlocks eight primary cells

so that vertices of the secondary cube are located at $\xi_i = \pm\frac{1}{2}$, $\eta_i = \pm\frac{1}{2}$, $\zeta_i = \pm\frac{1}{2}$. Thus, all vertices of the secondary cell are located at the centroids of the surrounding primary cells. Partial derivatives of x at the primary or secondary cell centres $\zeta = \xi = \eta = 0$ are calculated by formulae such as:

$$\begin{aligned}
(x_\xi)_{ijk} = 0.25(&x_{i-\frac{1}{2}\,j+\frac{1}{2}\,k-\frac{1}{2}} - x_{i-\frac{1}{2}\,j-\frac{1}{2}\,k-\frac{1}{2}} + x_{i+\frac{1}{2}\,j+\frac{1}{2}\,k-\frac{1}{2}} \\
&- x_{i+\frac{1}{2}\,j-\frac{1}{2}\,k-\frac{1}{2}} + x_{i-\frac{1}{2}\,j+\frac{1}{2}\,k+\frac{1}{2}} - x_{i-\frac{1}{2}\,j-\frac{1}{2}\,k+\frac{1}{2}} \\
&+ x_{i+\frac{1}{2}\,j+\frac{1}{2}\,k+\frac{1}{2}} - x_{i+\frac{1}{2}\,j-\frac{1}{2}\,k+\frac{1}{2}}) \\
(x_\eta)_{ijk} = 0.25(&-x_{i-\frac{1}{2}\,j-\frac{1}{2}\,k-\frac{1}{2}} - x_{i-\frac{1}{2}\,j+\frac{1}{2}\,k-\frac{1}{2}} + x_{i+\frac{1}{2}\,j+\frac{1}{2}\,k-\frac{1}{2}} \\
&+ x_{i+\frac{1}{2}\,j-\frac{1}{2}\,k-\frac{1}{2}} - x_{i-\frac{1}{2}\,j-\frac{1}{2}\,k+\frac{1}{2}} - x_{i-\frac{1}{2}\,j+\frac{1}{2}\,k+\frac{1}{2}} \\
&+ x_{i+\frac{1}{2}\,j+\frac{1}{2}\,k+\frac{1}{2}} + x_{i+\frac{1}{2}\,j-\frac{1}{2}\,k+\frac{1}{2}}) \\
(x_\zeta)_{ijk} = 0.25(&-x_{i-\frac{1}{2}\,j-\frac{1}{2}\,k-\frac{1}{2}} - x_{i-\frac{1}{2}\,j+\frac{1}{2}\,k-\frac{1}{2}} - x_{i+\frac{1}{2}\,j+\frac{1}{2}\,k-\frac{1}{2}} \\
&- x_{i+\frac{1}{2}\,j-\frac{1}{2}\,k-\frac{1}{2}} + x_{i-\frac{1}{2}\,j-\frac{1}{2}\,k+\frac{1}{2}} + x_{i-\frac{1}{2}\,j+\frac{1}{2}\,k+\frac{1}{2}} \\
&+ x_{i+\frac{1}{2}\,j+\frac{1}{2}\,k+\frac{1}{2}} + x_{i+\frac{1}{2}\,j-\frac{1}{2}\,k+\frac{1}{2}})
\end{aligned} \tag{9}$$

with similar expressions for the other partial derivatives of y, z, ϕ, ρhU, ρhV, ρhW if an assumption is made that each of these quantities can be expressed by equations similar to Eq (3). The spatial increments $\Delta\xi$, $\Delta\eta$, $\Delta\zeta$ are equal to 1 and, therefore, have been omitted.

The values for the i, j, k indices cover the whole computational grid. In particular i ranges from 2 (=suction surface) to IMP1 (=pressure surface), Fig 8, j ranges from 2 (=next after inlet plane) to JMM1 (=one before outlet plane), while k ranges from 2 (=hub) to KMP1 (=casing), Fig 7. Note that two independent index systems are used throughout the computational grid. Indices assigned with $\pm\frac{1}{2}$ denote grid points at the centres of the primary cells. The formula for the local flux balance, Eq (8), can be obtained by applying it to the secondary cells centered at i, j, k (Appendix 1). The discrete approximation is obtained by using the partial derivatives introduced previously.

This analysis completes the definition of the discrete approximation scheme for main stream points in subsonic flow; but the numerical formulation of the *transonic* problem requires the construction of an appropriate set of differential equations.

Problems encountered in the development of an efficient numerical algorithm for the calculation of transonic flows are:

(1) The equations governing the flow motion are non-linear.

(2) The flow is a mixed type with both subsonic and supersonic flows co-existing with the boundaries between them unknown.

(3) The solution will in general contain shock waves, the position of which is also unknown.

When the artificial compressibility method is applied, Appendix 2, the continuity equation becomes:

$$\frac{\partial}{\partial\xi}(\tilde{\rho}hU) + \frac{\partial}{\partial\eta}(\tilde{\rho}hV) + \frac{\partial}{\partial\zeta}(\tilde{\rho}hW) = 0 \tag{10}$$

where

$$\tilde{\rho} = \rho - \mu(\rho_s \Delta s) \tag{11}$$

$$\rho_s \Delta s = \frac{U}{Q}\delta_\xi \rho \, \Delta\xi + \frac{V}{Q}\delta_\eta \rho \, \Delta\eta + \frac{W}{Q}\delta_\zeta \rho \, \Delta\zeta \tag{12}$$

$$Q = (U^2 + V^2 + W^2)^{\frac{1}{2}} \tag{13}$$

$$\mu = \max\left[0, \left(-\frac{1}{M^2}\right)k\right] \tag{14}$$

k being typically 1.6, while upwind differencing is used in evaluating $\delta_\xi \rho \, \Delta\xi$, $\delta_\eta \rho \, \Delta_\eta$ and $\delta_\zeta \rho \, \Delta\zeta$ as follows:

$$\begin{aligned}
&\delta_\xi \rho \, \Delta\xi = \rho_{ijk} - \rho_{i,j-1,k} \quad \text{if } U_{ijk} > 0 \\
&\delta_\xi \rho \, \Delta\xi = \rho_{i,j+1,k} - \rho_{ijk} \quad \text{if } U_{ijk} \leq 0 \\
&\delta_\eta \rho \, \Delta\eta = \rho_{ijk} - \rho_{i-1j,k} \quad \text{if } V_{ijk} > 0 \\
&\delta_\eta \rho \, \Delta\eta = \rho_{i+1,j,k} - \rho_{ijk} \quad \text{if } V_{ijk} \leq 0 \\
&\delta_\zeta \rho \, \Delta\zeta = \rho_{ijk} - \rho_{i,j,k-1} \quad \text{if } W_{ijk} > 0 \\
&\delta_\zeta \rho \, \Delta\zeta = \rho_{ijk+1} - \rho_{ijk} \quad \text{if } W_{ijk} \leq 0
\end{aligned} \tag{15}$$

This scheme maintains an upwind influence in the differentiation for supersonic regions anywhere in the mesh for all possible orientations of the velocity vector. When the solution is converged the application of the mass conservation and energy equations to the series of interlocking finite volumes will yield zero net flux into each volume so that overall mass and energy are conserved.

Boundary conditions

Hub, casing, suction and pressure surface flows

Fig 4 shows the secondary boundary cell of the first computational plane $k = 2$ (hub) of the flowfield. Half the cell is hidden inside the hub surface. It is possible for a cell on the hub plane to be bounded on more than one face by solid boundaries (suction or pressure side).

When the flux balance is established on the secondary cell i, j, k the flux through the solid body (hub) must be zero.

$$\begin{aligned}
&(\rho hU)_{i-\frac{1}{2},j-\frac{1}{2},k-\frac{1}{2}} = 0 \qquad (\rho hU)_{i-\frac{1}{2},j+\frac{1}{2},k-\frac{1}{2}} = 0 \\
&(\rho hU)_{i+\frac{1}{2},j+\frac{1}{2},k-\frac{1}{2}} = 0 \qquad (\rho hU)_{i+\frac{1}{2},j-\frac{1}{2},k-\frac{1}{2}} = 0 \\
&(\rho hV)_{i-\frac{1}{2},j-\frac{1}{2},k-\frac{1}{2}} = 0 \qquad (\rho hV)_{i-\frac{1}{2},j+\frac{1}{2},k-\frac{1}{2}} = 0 \\
&(\rho hV)_{i+\frac{1}{2},j+\frac{1}{2},k-\frac{1}{2}} = 0 \qquad (\rho hV)_{i+\frac{1}{2},j-\frac{1}{2},k-\frac{1}{2}} = 0 \\
&(\rho hW)_{i-\frac{1}{2},j-\frac{1}{2},k-\frac{1}{2}} = 0 \qquad (\rho hW)_{i-\frac{1}{2},j+\frac{1}{2},k-\frac{1}{2}} = 0 \\
&(\rho hW)_{i+\frac{1}{2},j+\frac{1}{2},k-\frac{1}{2}} = 0 \qquad (\rho hW)_{i+\frac{1}{2},j-\frac{1}{2},k-\frac{1}{2}} = 0
\end{aligned} \tag{16}$$

where $i = 3$, IM, $j = 2$, JMM1, $k = 2$. The flux along the ζ direction at the $i, j, k + \frac{1}{2}$ grid point, lying in the flowfield, is taken over twice the area of the flux along either ξ or η directions.

The treatment of the casing surface, as well as of the blade suction and pressure sides, Fig 5, is based on a similar analysis.

Corner flows

Fig 6 shows a secondary cell bounded on two faces by solid boundaries. Half the cell is hidden in each of the two faces adjacent to the solid body. When the flux balance is established on the secondary cell i, j, k the flux through the solid body of the hub ($k = 2$) and that of the suction ($i = 2$) side must be zero.

The flux along the η and ζ directions at $i + \frac{1}{2}, j, k + \frac{1}{2}$ grid point, lying in the flowfield is taken over twice the area of the flux along the ξ direction.

The flow treatment for the hub-pressure, casing-suction, and casing-pressure corners is based on a similar analysis.

Shed vorticity, periodic boundaries and Kutta-Joukowski condition

It is assumed that the flow is identical in each blade passage of the machine so that only one passage needs to be considered. The inlet and outlet flow regions are divided by imaginary surfaces extended upstream and downstream from the blade leading and trailing edges, respectively, as shown in Fig 1. These extensions, which are assumed to be stream surfaces of the flowfield, are located at angular intervals $\Delta\theta = 2\pi/N$ with N being the number of blades in the machine.

The boundary conditions at the inlet plane surfaces ABEF(A'B'E'F') are only subject to the condition of periodicity specified by the equality of the complete velocity vector and the tangential velocity components at corresponding points of the two surfaces. If the tangential components of velocities at corresponding points in ABEF and A'B'E'F' are identical, the variation of the potential within each

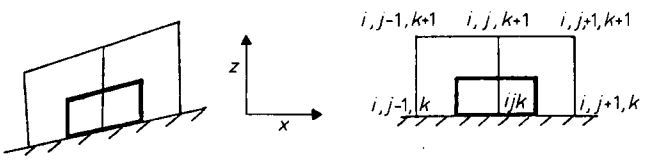

Fig 4 Boundary cell for the hub (casing) surfaces

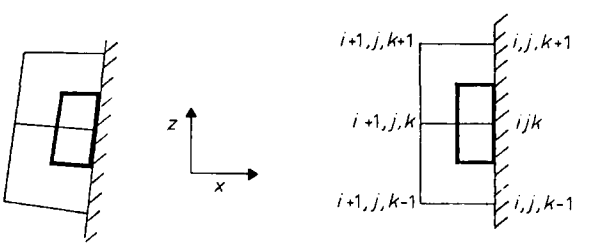

Fig 5 Boundary cell for the suction (pressure) sides

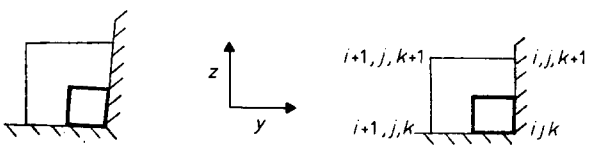

Fig 6 Boundary cell for the hub-section, hub-pressure, casing-suction, casing-pressure corner flows

surface is the same so that values of ϕ at corresponding points can differ only by a constant amount $\Delta\phi_{in}$. Thus, for periodic points:

$$\phi_{A'B'E'F'} = \phi_{ABEF} + \Delta\phi_{in} \quad (17)$$

where $\Delta\phi_{in}$ determines the mean whirl velocity at any radius for the inlet plane.

At the surfaces CDGH (C'D'G'H') formed by the extensions from the blade surfaces in the outlet region, the boundary conditions are also subject to a condition of periodicity specified by the equality of the magnitude of the velocity vector and the velocity components tangential to corresponding periodic points of the two successive stream surfaces: the grid lines lie along the mean streamlines (normal velocity components are zero). The condition of equal velocities tangential to the surfaces can be transformed into a relation containing ϕ:

$$\phi_{C'D'G'H'} = \phi_{CDGH} + \Delta\phi_{out}(k) \quad k = 2, 3, \ldots \text{KMP1} \quad (18)$$

The inclusion of variable potential jump $\Delta\phi_{out}(k)$ combined with the complete equality of the velocity vectors yields velocities along the vortex sheet perpendicular to the mean streamline, equal in magnitude but opposite in direction at the corresponding periodic points of CDGH(C'D'G'H') surfaces. The $\Delta\phi_{out}(k)$ must be found through an iterative procedure so as to satisfy the Kutta condition in the blades which demands equal pressures to be obtained at the control points of the elements adjacent to the trailing edges. Unfortunately, when the downstream stream surfaces carry vorticity their position and the magnitude of $\Delta\phi_{out}(k)$ become significant in determining the velocity distribution. The current code places the vortex surfaces in predetermined positions, coinciding with the exit periodic surfaces while the $\Delta\phi_{out}(k)$ is held constant along grid lines which are chosen to lie in the expected stream direction; however, it may take different values at different points across the trailing edge span. It is the inclusion of this approximate treatment of the vortex sheet that allows the current code to arrive at realistic values for variation of the blade circulation along the blade span.

The potential on the inlet periodic boundary A'B'E'F' is calculated by:

$$\phi_{IMP1,j,k} = \phi_{2,j,k} + \Delta\phi_{in} \quad (19)$$

with

$$\Delta\phi_{in} = pv_1 \quad (20)$$

where p is the cascade pitch and v_1 the whirl velocity at inlet.

On the outlet periodic boundary C'D'G'H' the potential is given by:

$$\phi_{IMP1,j,k} = \phi_{2,j,k} + \Delta\phi_{out}(k) \quad (21)$$

where

$$\Delta\phi_{out}(k) = \phi_{IMP1,JTEP1,k} - \phi_{2,JTEP1,k} \quad (22)$$

with JTEP1 = JTE + 1, JTE is the last pitchwise computational line on the blade surface and:

$$\phi_{IMP1,JTEP1,k} = \phi_{IMP1,JTEM1,k} + \frac{q_{2,JTE,k}}{q_{IMP1,JTE,k}} (\phi_{IMP1,JTEP1,k} - \phi_{IMP1,JTEM1,k}) \quad (23)$$

with JTEM1 = JTE − 1.

All potential jump values, $\Delta\phi_{in}$ and $\Delta\phi_{out}(k)$ are relaxed before they are used to yield the 'upper' periodic boundary values.

For situations involving non-lifting as well as for nozzle flows the current version of the computer code bypasses the whole potential jump evaluation process.

Complex geometry mesh generation

A complex grid system was developed and implemented on the main numerical method to allow cascade flows for blades of variable chord, twist, and cross-section to be calculated. An example of a complex geometry is shown in Fig 7. Blade cross-sections are measured at various radial (spanwise) positions. Each input cross-section is obtained from axial, suction surface and blade thickness co-ordinates allowing the blade shape to be properly described. Hub and casing radial co-ordinates along the machine axis are also provided as an input to computer code. Input cross-sections are interpolated to calculate the axial, suction surface and blade thickness co-ordinates on the requested kth cross-section. Thereafter,

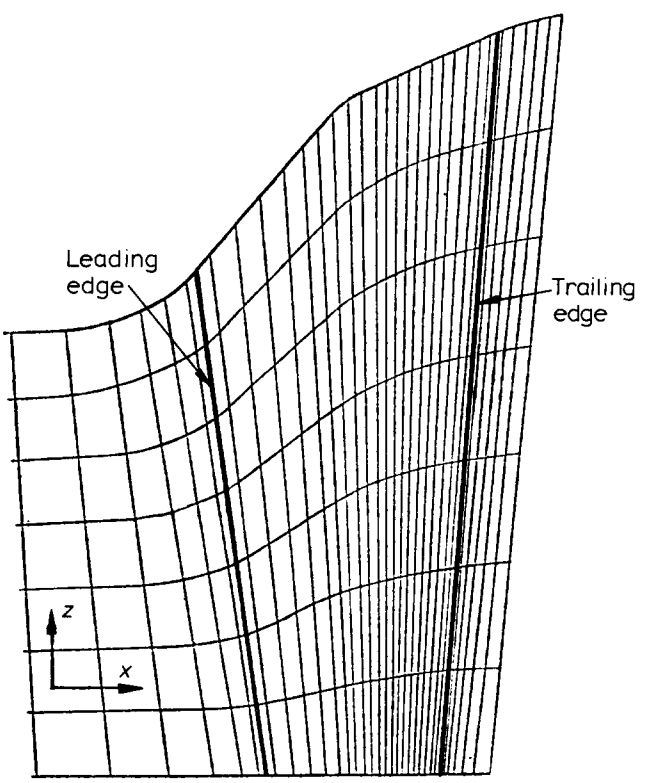

Fig 7 Intersection of the 3-D grid with the meridional plane

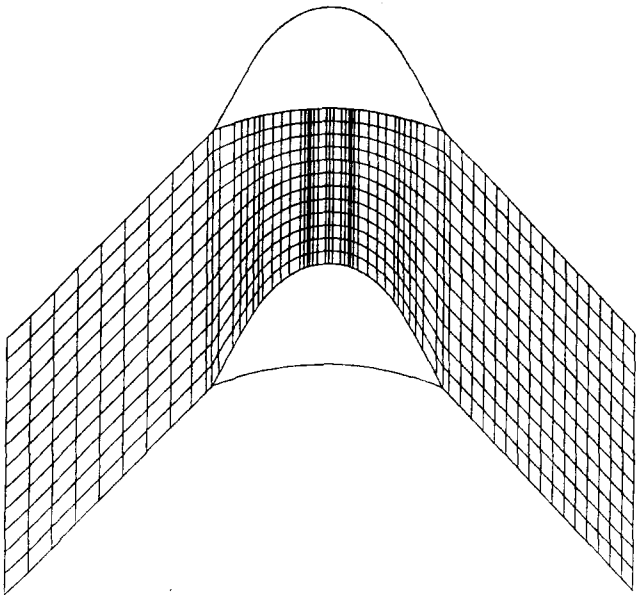

Fig 8 Intersection of the 3-D grid with the blade-to-blade plane

interpolations are used to locate the meridional grid points which are uniformly spaced in the z-direction. For linear cascade geometries the hub and tip radii are set to large values, such that the difference between them is the blade span (height), their ratio being close to unity, while the angular blade distance $2\pi/N$ multiplied by the mean span radius yields the cascade pitch.

The calculation of the blade-to-blade grid points containing the tangential and axial variations, is based on similar principles to those described in 2-D flow analysis, shown in Fig 8, while provision is made for the pitch variation along the radial direction for annular cascades.

The chosen grid is the simplest possible formation for numerical calculations in cascade problems. Use of pitchwise lines greatly simplifies the application of the periodic boundary properties between the bounding quasi-streamlines of the blade passage. However, the numerical scheme can be used with any grid formation which need not be uniformly spaced in any co-ordinate direction. The grid is not restricted to that shown. Any mesh generation technique can be adopted provided grid periodicity is maintained.

Numerical resolution, error assessment

A numerical algorithm has been designed for transonic flow calculation in turbomachinery blade rows with complex geometry. The current research version of the computer code which solves the governing flow equation on a body fitted computational grid points, uses point over-relaxation (SOR Gauss–Seidel).

Iterations were continued until the average change of axial velocity between successive iterations were <0.01%. Run time per point per iteration was 4.88×10^{-4} s, on an IBM 370-165 computer. Total number of iterations required for convergence was about 200 depending upon the geometry complexity (cascade-nozzle) and type of flow (subsonic-transonic). Total CPU time for a $7\times50\times7$ grid points mesh was ~3–4 min.

The finite-volume scheme is very stable and numerical experimentation has shown that the iterations will always converge within the limitations imposed by the assumptions.

The method described is very easy to program as the whole code has been developed by subroutine sections to facilitate assemblage of the numerical scheme. A total of 16 3-D arrays were used but this number can be reduced considerably though more computation time may be necessary to achieve the same convergence in the solution (Jameson[1]). The input data is very simple; thus, only the blade geometry and flow conditions need to be changed for each run. Many other forms of discrete approximation of the partial differential equations can be selected, by altering the order of the finite elements involved; however, if a simple adequate discrete approximation is chosen, higher accuracy must not be obtained through development of a higher-order partial differential approximation because this would complicate the numerical code developments whilst yielding only marginal benefits. With the present code there is sufficient flexibility for special regions of fine mesh to occur where resolution is otherwise inadequate due to steep gradients in the dependent variable. It is thus possible for the mesh density distribution to be chosen so that sufficient points in each co-ordinate direction are located in the region of steep gradient.

Errors could be generated by forcing the vorticity trailed by the blades to follow their geometrical direction instead of the outlet flow. It seems probable that this will have little effect on the distribution of the blade Mach number except close to the trailing edge region although some alterations are expected for the determination of the actual back pressure ratio.

As the flow becomes increasingly supersonic, the scheme is increasingly retarded in the upwind direction. The choice of factor k in the equation $\mu = \max\,[0, (1-a^2/q^2)\mathrm{k}]$ affects the accuracy of the solution significantly but not the stability of the scheme. Errors associated with values of the factor $\mathrm{k} > 1.6$ are increased Mach numbers in the subsonic regions of the blade suction surface while for supersonic regions, on the same blade surface, the Mach number is significantly decreased. The most common source of inaccuracy arises at a blunt leading edge where a relatively coarse grid cannot resolve adequately the rapid changes in the flow properties. To obtain an accurate solution around a blunt leading edge a large number of grid points must be used. This would cause no extra problems because the computer code automatically takes into account the increased number of grid points while the stability of the numerical scheme is hardly affected; however, the computer storage and the execution time will be increased.

In a very limited number of tests it was found necessary to smooth the potential in axial pitchwise and radial directions before it was used in the next

iteration. When a solution of the potential at any point is sought, the numerical scheme can lead to two independent solutions i.e. one solution for the odd points and another for the even points, thus producing a wavy distribution of the potential. This problem has been solved previously[1] by adding extra compensating flux terms on all cell faces thus producing a formula which can lead to the usual five-point second-order-accurate scheme or to the nine-point fourth-order-accurate scheme. In the present numerical code a first-order smoothing process helps to overcome the wavy distribution of the potential.

Applications

Bent convergent–divergent nozzle

The nozzle is constructed of two circular arcs. At the axial distance of 7.5 cm the nozzle height attains a minimum value of 2.5 cm which is half the inlet height. Between axial distances of 7.5 cm and 13.5 cm the height has been designed to give constant cross-sectional flow area of 12.5 cm^2 while for distances <7.5 cm and >13.5 cm the nozzle height is smoothly increased to meet the required cross-sectional area for the inlet, 25.0 cm^2, and the outlet,

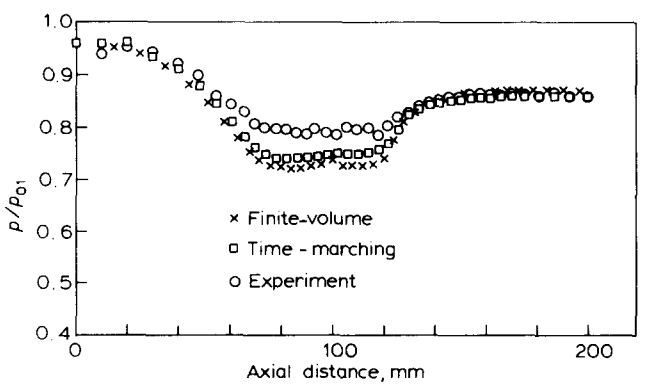

Fig 9 Comparison between measured, time-marching solution and finite-volume solution pressure distribution in the flat-convex corner for the bent convergent–divergent nozzle at $P_2/P_{01} = 0.86$ (experimental)

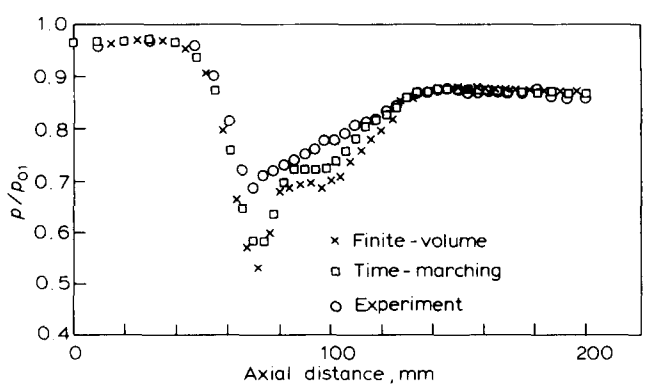

Fig 10 Comparison between measured, time-marching solution and finite-volume solution pressure distribution in the curved convex corner for the bent convergent–divergent nozzle at $P_2/P_{01} = 0.86$ (experimental)

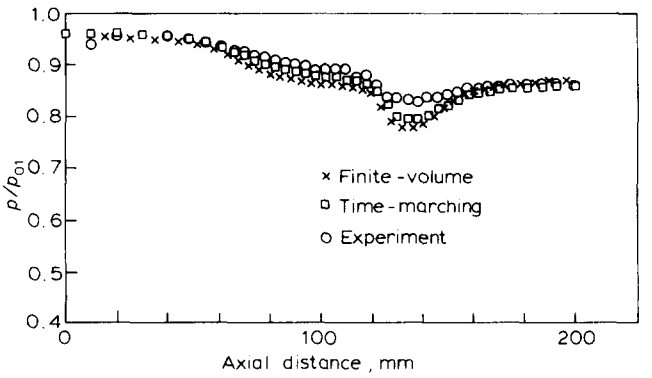

Fig 11 Comparison between measured, time-marching solution and finite-volume solution pressure distribution in the flat-concave corner for the bent convergent–divergent nozzle at $P_2/P_{01} = 0.86$ (experimental)

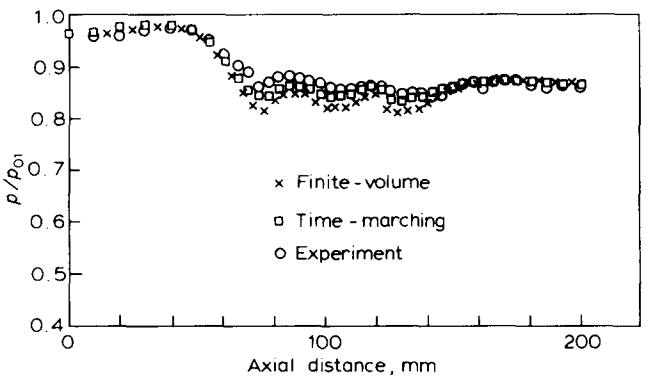

Fig 12 Comparison between measured, time-marching solution and finite-volume solution pressure distribution in the curved-concave corner for the bent convergent–divergent nozzle at $P_2/P_{01} = 0.86$ (experimental)

15.0 cm^2. A total flow turning angle of 60° was required which is about the minimum level of turning for turbine nozzles.

Two numerical methods were used to predict the flowfield in the bent convergent–divergent nozzle: (1) the current 3-D finite-volume which solves the full potential equation, and (2) Denton's[4] fully 3-D method which solves the Euler equations.

Both methods use similar input data. Simulation of flat end wall surfaces requires large values of hub and casing radii to be specified such that the difference between them yields the nozzle height at any axial location. The radius ratio must be close to unity while the number of blades is set to give the required cascade pitch (5 cm). With such an arrangement the convex and concave sides will be almost perpendicular to the flat (hub) and curved (casing) surfaces of the nozzle. The computational grid was formed by finite-volume elements of $\Delta x : \Delta y : \Delta z \sim 1 : 1 : 1$. The current test modelling has been carried out with a $7 \times 40 \times 7$ grid points mesh.

Comparison of the experimental pressure distribution with the numerical methods, the measured back pressure ratio being 0.86 for each of the nozzle corners, is shown in Figs 9–12.

Predicted results indicate that to improve the comparison with the experiment a higher back pressure should have been used. For subsonic flow, contraction of the flow cross-sectional area increases the flow speed and thus reduces the static pressure. An inviscid numerical solution predicts the flow without any boundary layer developments. Cross-sectional flow area coincides with the geometrical cross-section; therefore, direct comparison between calculated and measured pressures on the nozzle surface using the same back pressure may produce unsatisfactory results.

The agreement between the predicted and measured static pressures is generally satisfactory. Peak Mach number location in the curved-convex corner, Fig 10, is in good agreement with the experimental position, but not its actual value because of the viscous effects previously mentioned.

Dawes thin-thick-thin aerofoil

A version of the NASA series 34 aerofoil was manufactured and tested at various exit flow conditions by Dawes[5]. It was made to assess the effect of the 3-D flow on simple geometries. At mid-span the aerofoil was of maximum thickness (12%) of the blade chord (thick) while at each of the two tips the maximum thickness was only 6% of the chord (thin). Diagrammatic aerofoil and working section arrangements are shown in Fig 13.

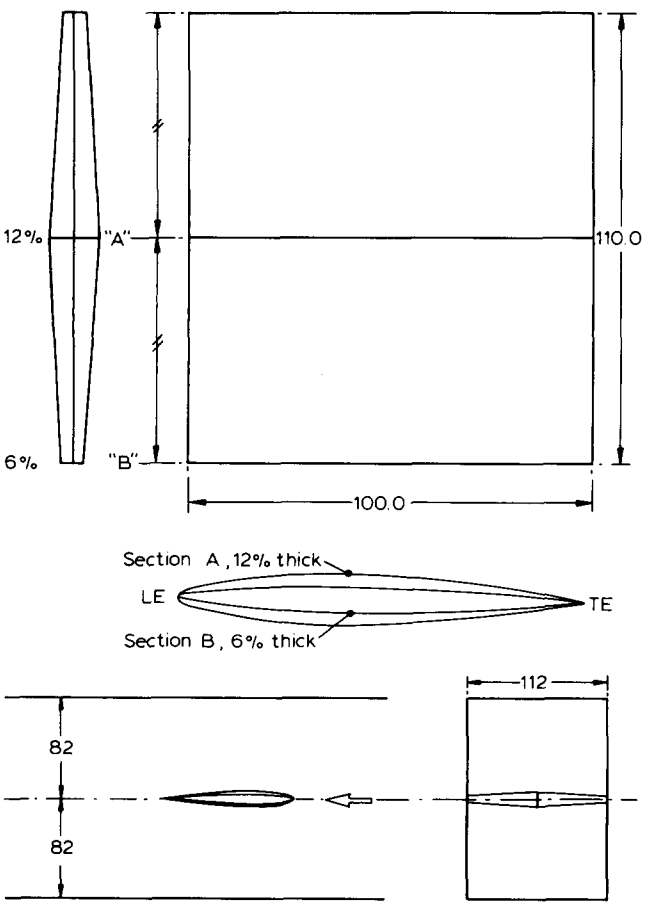

Fig 13 Dawes' 'thin-thick-thin' aerofoil and working section arrangements. All dimensions in mm

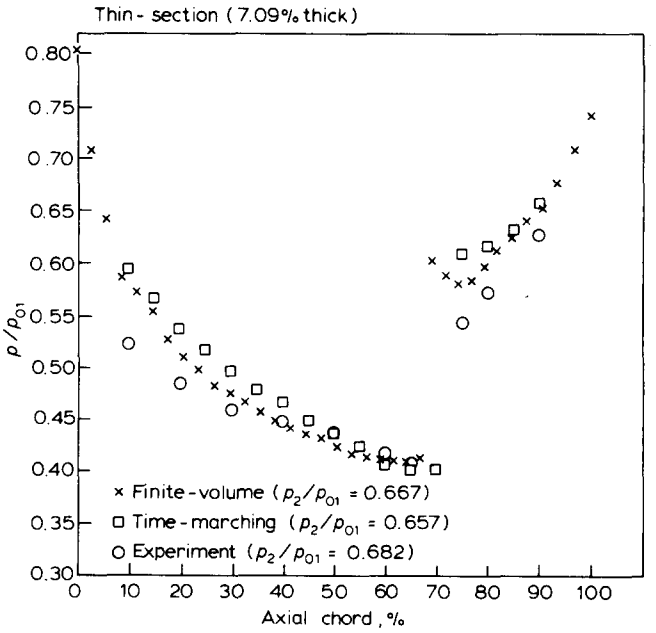

Fig 14 Comparison between measured, time-marching solution and finite-volume solution for blade pressure distribution on the 'thin' section of the 'thin-thick-thin' aerofoil

For computational analysis the finite-volume grid mesh $7\times50\times7$ was extended half a chord up and downstream from the aerofoil leading and trailing edges, respectively. Each blade pitch was equal to the width (162 mm) of the working space tunnel, while the blade span was 112 mm. Due to the inherent symmetry of the thin-thick-thin blade and to save computing time the span and pitch sizes actually used were only half of these figures and, therefore, the computed section was only one quarter of the total available geometry. A comparison with Denton's method was made at exit flow conditions, the experimental back pressure being 0.682. Agreement between theories and experiment is satisfactory on both the 'thin' or the 'thick' blade sections, shown in Figs 14 and 15, respectively. Disagreement between theories and experiment in the region downstream to the shock is probably largely due to viscous effects in the experiment.

NASA nozzle annular turbine cascade

Goldman and McLallin[6] have tested a fully annular cascade of gas turbine blades, where 3-D effects could be obtained. The annular cascade consists of 36 untwisted blades with a constant cross-section profile from hub-to-tip, an axial chord of 3.823 cm and height of 3.81 cm. The mean blade radius is 23.5 cm while the pitch to axial chord ratio is 1.07 at mid-height. Blade surface pressure distributions have been measured at three blade heights. One blade was instrumented with 20 tappings located at the mean radius. The second blade had 11 tappings located 0.51 cm from the blade hub with a similar arrangement for the blade casing. Fig 16 compares measured and calculated Mach number distributions when the calculated exit plane averaged $M_2=0.761$ and the measured $M_2=0.756$. The agreement

between theory and experiment is satisfactory despite the secondary flow effects in this 3-D flow region. These viscous effects cause high total pressure losses and subsequently loss of cascade efficiency. Similar satisfactory agreement is also obtained on the blade mid-height where the viscous losses are substantially lower than on the hub, Fig 17. At the blade tip, Fig 18, the agreement continues to be good on suction and pressure blade surfaces. Calculated hub and tip Mach numbers are referred to a location 0.31 cm from the cascade hub and casing, respectively.

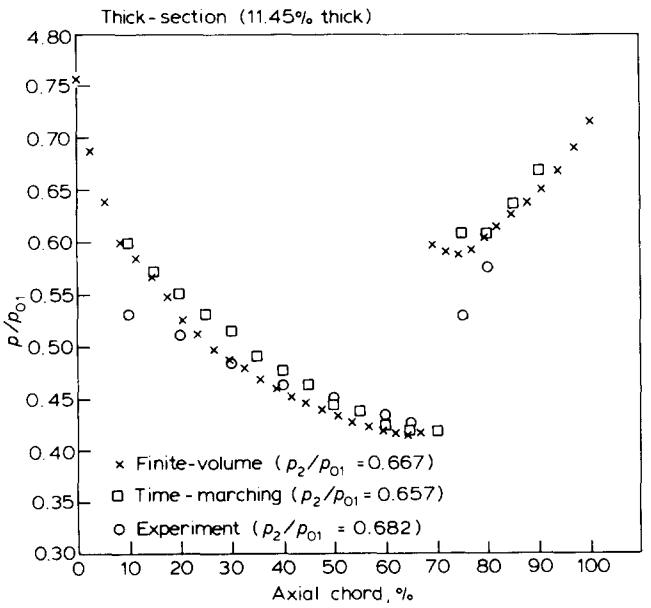

Fig 15 Comparison between measured, time-marching solution and finite-volume solution for blade pressure distribution on the 'thick' section of the 'thin-thick-thin' aerofoil

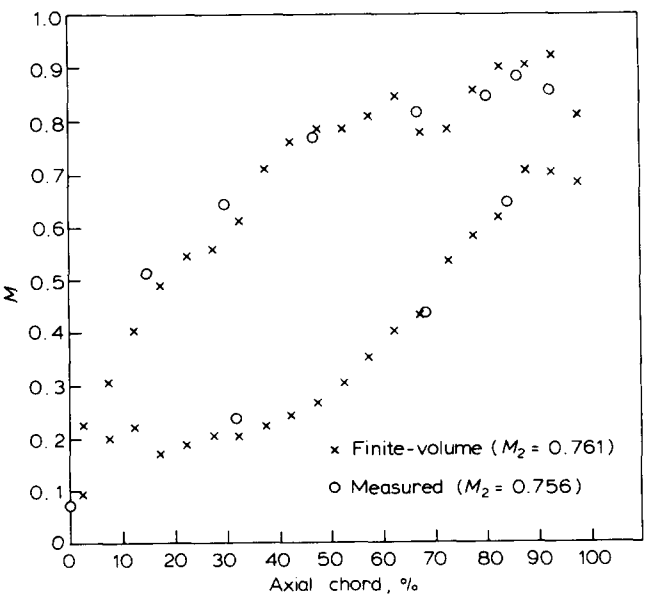

Fig 16 Comparison between measured and finite-volume predicted blade Mach number distribution at hub for the NASA nozzle annular turbine cascade

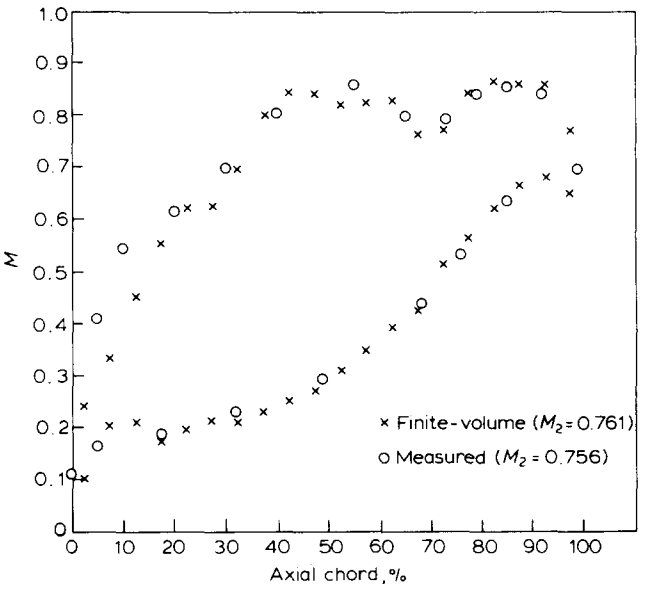

Fig 17 Comparison between measured and finite-volume predicted blade Mach number distribution at mid-span for the NASA nozzle annular turbine cascade

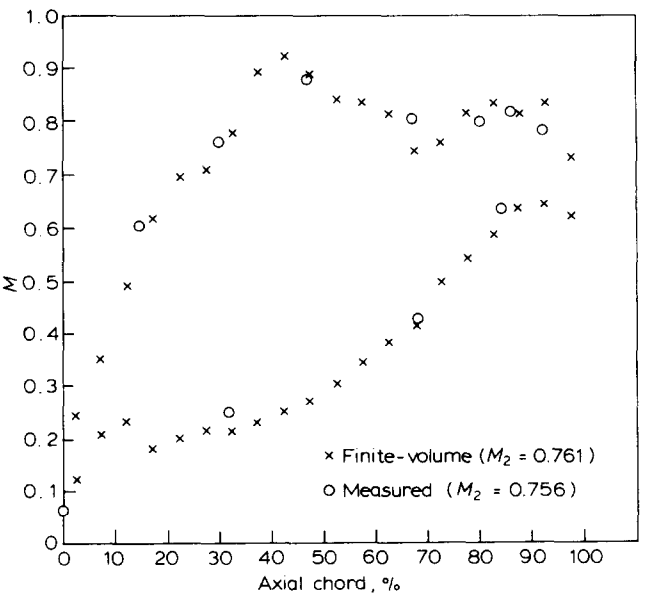

Fig 18 Comparison between measured and finite-volume predicted blade Mach number distribution at casing for the NASA nozzle annular turbine cascade

Conclusion

A finite-volume method has been developed for the calculation of transonic, potential flows through 3-D turbomachinery blades with complex geometries. The method combines the advantages of the use of finite-elements for handling complicated geometries with the use of simple finite-difference approximations. It uses a first-order shape function and is based on a numerical scheme similar to that developed for 2-D flows[3]. The main advantage of the numerical scheme is that it offers an accurate approximation of

the geometrically complex turbomachinery solid boundaries, while the actual implementation of the boundary conditions is straightforward. For transonic flows the mixed type non-linear equations are treated by constructing a central difference approximation to the differential equation and by adding an artificial compressibility term to the density (upwind density gradient) to produce the desired directional bias in the hyperbolic region. The most common source of inaccuracy arises at a blunt leading edge where the relatively coarse grid cannot resolve adequately the rapid changes in the flow properties. Errors can be generated by forcing the vorticity trailed by the blades to follow their geometrical direction instead of the outlet flow. A close alignment between the expected vortex sheets and the extended periodic stream surfaces is recommended if realistic results are to be obtained. When flow incidence effects on the cascade of blades are sought then it is necessary to alter the pitchwise co-ordinates, upstream from the leading edges, so as to be compatible with the new flow angle. Finally, it must be emphasized that the finite volume calculations are made by specifying a fixed potential difference between the cascade inlet and outlet sections. Therefore, it is not known *a priori* which back pressure the specified potential difference will produce when the solution is converged. In the present analysis under the isentropic assumption the normal component of momentum is not conserved through the shock wave and although this introduces small errors in transonic regions ($M \leq 1.3$) it does not apply to high supersonic shocked flows, though it can yield satisfactory results in the shock-free supersonic region. The computing case is being extended to include (1) rotating cascade and (2) supersonic inlet Mach numbers. Comparison of the calculated results with experiment and/or with Denton's fully 3-D inviscid numerical method for various turbomachinery configurations indicates that the 3-D finite volume approach is an accurate, reliable and relatively fast, (compared to other inviscid solutions), method for the prediction of inviscid, transonic potential flow through turbomachinery blade rows. It may form the basis for numerous fluid dynamic developments in turbomachinery.

References

1. **Jameson A. and Caughey D. A.** A finite volume method for transonic potential flow equations. *AIAA Paper No. 77-635 October 1977*
2. **Holst T. L.** A fast conservative algorithm for solving the transonic full potential equation. *AIAA Paper No. 79-1456, 1979*
3. **Soulis J. V.** Calculation of transonic potential flow through turbomachinery blade rows. *Ph.D. Thesis Cambridge University, January 1982*
4. **Denton J. D.** A time-marching method for two and three dimensional blade to blade flows. *Aeronautical Research Council, R. & M. 3775, 1975*
5. **Dawes W. N.** A study of shock waves in three-dimensional transonic flow. *Ph.D. Thesis Cambridge University, September 1979*
6. **Goldman L. H. and McLallin K. L.** Cold air annular cascade investigations of aerodynamic performance of core-engine cooled turbine vanes. *NASA TM X-3223, 1975*
7. **Hafez M. M., Murmann E. M. and South J. C.** Artificial compressibility methods for numerical solution of transonic full potential equation. *AIAA Paper No. 78-1148, July 1978*

Appendix 1

The flux balance, Eq (8), when it is applied to the secondary cell centred at i, j, k yields:

$$
\begin{aligned}
&(\rho hU)_{i-\frac{1}{2},j+\frac{1}{2},k-\frac{1}{2}} - (\rho hU)_{i-\frac{1}{2},j-\frac{1}{2},k-\frac{1}{2}} \\
&+(\rho hU)_{i+\frac{1}{2},j+\frac{1}{2},k-\frac{1}{2}} - (\rho hU)_{i+\frac{1}{2},j-\frac{1}{2},k-\frac{1}{2}} \\
&+(\rho hU)_{i-\frac{1}{2},j+\frac{1}{2},k+\frac{1}{2}} - (\rho hU)_{i-\frac{1}{2},j-\frac{1}{2},k+\frac{1}{2}} \\
&+(\rho hU)_{i+\frac{1}{2},j+\frac{1}{2},k+\frac{1}{2}} - (\rho hU)_{i+\frac{1}{2},j-\frac{1}{2},k+\frac{1}{2}} \\
&-(\rho hV)_{i-\frac{1}{2},j-\frac{1}{2},k-\frac{1}{2}} - (\rho hV)_{i-\frac{1}{2},j+\frac{1}{2},k-\frac{1}{2}} \\
&+(\rho hV)_{i+\frac{1}{2},j+\frac{1}{2},k-\frac{1}{2}} + (\rho hV)_{i+\frac{1}{2},j-\frac{1}{2},k-\frac{1}{2}} \\
&-(\rho hV)_{i-\frac{1}{2},j-\frac{1}{2},k+\frac{1}{2}} - (\rho hV)_{i-\frac{1}{2},j+\frac{1}{2},k+\frac{1}{2}} \\
&+(\rho hV)_{i+\frac{1}{2},j-\frac{1}{2},k+\frac{1}{2}} + (\rho hV)_{i-\frac{1}{2},j-\frac{1}{2},k-\frac{1}{2}} \\
&-(\rho hW)_{i-\frac{1}{2},j-\frac{1}{2},k-\frac{1}{2}} - (\rho hW)_{i-\frac{1}{2},j+\frac{1}{2},k-\frac{1}{2}} \\
&-(\rho hW)_{i+\frac{1}{2},j+\frac{1}{2},k-\frac{1}{2}} - (\rho hW)_{i+\frac{1}{2},j-\frac{1}{2},k-\frac{1}{2}} \\
&+(\rho hW)_{i-\frac{1}{2},j-\frac{1}{2},k+\frac{1}{2}} + (\rho hW)_{i-\frac{1}{2},j+\frac{1}{2},k+\frac{1}{2}} \\
&+(\rho hW)_{i+\frac{1}{2},j+\frac{1}{2},k+\frac{1}{2}} + (\rho hW)_{i+\frac{1}{2},j-\frac{1}{2},k+\frac{1}{2}} = 0 \qquad (1.1)
\end{aligned}
$$

The quantities ρ, h, U, V, W are all calculated at the centres of the primary cells surrounding the secondary cell centred at i, j, k. Approximations of the local velocity U, V and W at the centre, eg $i+\frac{1}{2}$, $j+\frac{1}{2}$, $k+\frac{1}{2}$ of a primary cell are:

$$
\begin{aligned}
U_{i+\frac{1}{2},j+\frac{1}{2},k+\frac{1}{2}} &= \left[g^{11}\frac{\partial\phi}{\partial\xi} + g^{12}\frac{\partial\phi}{\partial\eta} + g^{13}\frac{\partial\phi}{\partial\zeta}\right]_{i+\frac{1}{2},j+\frac{1}{2},k+\frac{1}{2}} \\
V_{i+\frac{1}{2},j+\frac{1}{2},k+\frac{1}{2}} &= \left[g^{21}\frac{\partial\phi}{\partial\xi} + g^{22}\frac{\partial\phi}{\partial\eta} + g^{23}\frac{\partial\phi}{\partial\zeta}\right]_{i+\frac{1}{2},j+\frac{1}{2},k+\frac{1}{2}} \\
W_{i+\frac{1}{2},j+\frac{1}{2},k+\frac{1}{2}} &= \left[g^{31}\frac{\partial\phi}{\partial\xi} + g^{32}\frac{\partial\phi}{\partial\eta} + g^{33}\frac{\partial\phi}{\partial\zeta}\right]_{i+\frac{1}{2},j+\frac{1}{2},k+\frac{1}{2}}
\end{aligned} \qquad (1.2)
$$

Thus, the discrete approximation of the governing flow equation in the local co-ordinate system is:

$$
\begin{aligned}
&a_1\phi_{i-1,j-1,k-1} + a_2\phi_{i-1,j+1,k+1} + a_3\phi_{i+1,j+1,k-1} \\
&+a_4\phi_{i+1,j-1,k-1} + a_5\phi_{i-1,j-1,k+1} + a_6\phi_{i-1,j+1,k+1} \\
&+a_7\phi_{i+1,j+1,k+1} + a_8\phi_{i+1,j-1,k+1} + a_9\phi_{i-1,j-1,k} \\
&+a_{10}\phi_{i-1,j+1,k} + a_{11}\phi_{i+1,j+1,k} + a_{12}\phi_{i+1,j-1,k} \\
&+a_{13}\phi_{i-1,j,k-1} + a_{14}\phi_{i-1,j,k+1} + a_{15}\phi_{i+1,j,k-1} \\
&+a_{16}\phi_{i+1,j,k+1} + a_{17}\phi_{i,j+1,k-1} + a_{18}\phi_{i,j,k+1} \\
&+a_{19}\phi_{i,j-1,k+1} + a_{20}\phi_{i,j-1,k-1} + a_{21}\phi_{i-1,j,k} \\
&+a_{22}\phi_{i,j+1,k} + a_{23}\phi_{i+1,j,k} + a_{24}\phi_{i,j-1,k} \\
&+a_{25}\phi_{i,j,k+1} + a_{26}\phi_{i,j,k-1} + a_{27}\phi_{i,j,k} = 0 \qquad (1.3)
\end{aligned}
$$

where the weighting coefficients $a_1, a_2, a_3, \ldots, a_{25}, a_{26}, a_{27}$ are functions of ρ, g^{ij} and h. Note that the geometrical coefficients, the determinant of the transformation and the densities are all calculated at the primary cell centroids while a potential ϕ is assigned to each vertex of the eight primary cells surrounding the secondary cell centroid.

Appendix 2

For 2-D full potential equations the corresponding 'viscous' transonic flow equation can be written (Hafez *et al.*[7]):

$$-\frac{\rho}{a^2}[(a^2-q^2)\phi_{ss}+a^2\phi_{nn}]=\frac{\rho}{a^2}\Delta s(a^2-q^2)\phi_{sss} \quad (2.1)$$

where s and n are co-ordinates in the local stream and normal directions, but the R.H.S. equals:

$$\frac{\rho}{a^2}\Delta s(a^2-q^2)\left[\frac{u}{q}\left(\frac{u^2u_x+2uvv_x+v^2v_y}{q^2}\right)_x \times\frac{v}{q}\left(\frac{u^2u_x+2uvu_y+v^2v_y}{q^2}\right)\right] \quad (2.2)$$

because

$$\phi_{sss}=\frac{u}{q}(\phi_{ss})_x+\frac{v}{q}(\phi_{ss})_y$$

and

$$\phi_{ss}=\frac{u^2}{q^2}\phi_{xx}+\frac{2uv}{q^2}\phi_{xy}+\frac{v^2}{q^2}\phi_{yy}$$

when these theories are extended to 3-D flows an artificial compressibility term arises in the mass flux equation:

$$-\frac{\rho}{a^2}\Delta s(a^2-q^2)\times \times\left[\frac{u}{q}\left(\frac{u^2u_x+2uvv_x+2uww_x+2vwv_z+v^2v_y+w^2w_z}{q^2}\right)_x +\frac{v}{q}\left(\frac{u^2u_x+2uvu_y+2uwu_z+2vww_y+v^2v_y+w^2w_z}{q^2}\right)_y +\frac{w}{q}\left(\frac{u^2u_x+2uvu_y+2uwu_z+2vwv_z+v^2v_y+w^2w_z}{q^2}\right)_z\right] \quad (2.3)$$

The first bracketed term is written as:

$$-\left(-\frac{\rho}{a^2}\right)\Delta s\left(1-\frac{a^2}{q^2}\right)q^2 \left[\frac{u}{q}\left(\frac{u^2u_x+2uvv_x+2uww_x+2vwv_z+v^2v_y+w^2w_z}{q^2}\right)_x\right]$$

An equivalent expression is given by:

$$-\left[\mu u\,\Delta s\left(\frac{u}{q}\rho_x+\frac{v}{q}\rho_y+\frac{w}{q}\rho_z\right)\right]_x$$

or $-(\mu u\rho_s\,\Delta s)_x$ where

$$\mu=\left(1-\frac{a^2}{q^2}\right) \quad (2.4)$$

$$\rho_x=-\frac{\rho}{a^2}(uu_x+vv_x+ww_x)$$

$$\rho_y=-\frac{\rho}{a^2}(uu_y+vv_y+ww_y) \quad (2.5)$$

$$\rho_z=-\frac{\rho}{a^2}(uu_z+vv_z+ww_z)$$

Similarly the second and the last members of the bracket yields:

$$-(\mu v\rho_s\,\Delta s)_y \qquad -(\mu w\rho_s\,\Delta s)_z$$

Thus, the continuity equation can be written as:

$$(\rho u)_x+(\rho v)_y+(\rho w)_z-(\mu u\rho_s\,\Delta_s)_x -(\mu v\rho_s\,\Delta_s)_y-(\mu w\rho_s\,\Delta_s)_z=0 \quad (2.6)$$

or

$$(\tilde{\rho}u)_x+(\tilde{\rho}v)_y+(\tilde{\rho}w)_z=0 \quad \text{with } \tilde{\rho}=\rho-\mu\rho_s\,\Delta_s$$